A. Abbà, D. Campaniello, M. Nini
Filter Size Definition in Anisotropic Subgrid Models for Large Eddy Simulation on Irregular Grids
Journal of Turbulence, Vol. 18, N. 6, 2017, p. 589-610
doi:10.1080/14685248.2017.1312001

ARTICLE

Filter size definition in anisotropic subgrid models for Large Eddy Simulation on irregular grids

Antonella Abbà[a], Dario Campaniello[a], and Michele Nini[a]

[a]Dipartimento di Scienze e Tecnologie Aerospaziali, Politecnico di Milano, Via La Masa 34, 20156 Milano, Italy

ARTICLE HISTORY
Compiled March 23, 2017

Keywords: Turbulence modeling, Large Eddy Simulation, Discontinuous Galerkin methods, compressible flows, dynamic models.

AMS Subject Classification: 65M60, 65Z05, 76F25, 76F50, 76F65

CONTACT A. Abbà Email: antonella.abba@polimi.it

ABSTRACT
The definition of the characteristic filter size to be used for subgrid scales models in Large Eddy Simulation using irregular grids, is still an unclosed problem. We investigate some different approaches to the definition of the filter length for anisotropic subgrid scale models and we propose a tensorial formulation based on the inertial ellipsoid of the grid element. The results demonstrate an improvement in the prediction of several key features of the flow when the anisotropicity of the grid is explicitly taken into account with the tensorial filter size.

KEYWORDS
Large eddy simulation; subgrid model; anisotropic model; Discontinuous Galerkin.

1. Introduction

Nowadays, thanks to the increasing availability of large computational resources and the development of efficient numerical codes, large eddy simulation (LES) is more and more used for industrial, engineering and environmental applications. In realistic conditions of practical interest, a turbulent flows is characterized by complex geometries and by a complex dynamics involving a wide range of scales. The fundamental idea of LES is to directly simulate the turbulence scales larger than a given size, while the effects of the smaller scales, is provided by a closure model. For this purpose a filter is applied to the Navier-Stokes equations. A space filter extracts a large scales quantity $\overline{\phi}$ as follow:

$$\overline{\phi}(\mathbf{x}) = \int_{\Omega} G_{\overline{\Delta}}(\mathbf{x}, \boldsymbol{\xi}) \phi(\boldsymbol{\xi}) d\boldsymbol{\xi}. \tag{1}$$

Here $\overline{\Delta}$ denotes the filter size related to the kernel $G_{\overline{\Delta}}$ and Ω is the domain of the flow. In the most diffused approach any explicit filter isn't applied to the equation which are implicitly filtered over the numerical grid. This procedure is equivalent to the imposition of a top-hat filter with cutoff length $\overline{\Delta}$ related to the space resolution and to the grid element size Ω_e. Thus the side element size Δ is assumed as cutoff length when a cartesian grid with uniform spacing is used to discretize the equations.

The most common procedure to model the unresolved scales introduces a subgrid stress tensor based on the eddy viscosity concept in the equations of motion. The Smagorinsky model [1]

$$\tau_{ij} - \frac{1}{3}\tau_{kk} = -2\nu_{SGS}\overline{S}_{ij} = -2C_S\overline{\Delta}^2|\overline{S}|\overline{S}_{ij}$$

is the best-known example of eddy viscosity models which relies the subgrid stress tensor τ to the strain rate tensor $\overline{S}$ of the resolved velocity field. It requires that the Smagorinsky coefficient C_S and the filter size $\overline{\Delta}$ are imposed. The Smagorinsky model is often used in the dynamic formulation [2] determining the Smagorinsky coefficient in function of the resolved velocity field. The Smagorinsky model and, more in general, all the models based on a scalar eddy viscosity, are developed in the Kolmogorov hypothesis of isotropicity of the small turbulent scales. Instead it is well known that not only the large turbulent structures are not isotropic, but the unresolved turbulent eddies too.

Non isotropic grids are usually used in simulations of non homogeneous flows with the aim to better capture the large anisotropic turbulent structures. Moreover

anisotropic grids are also imposed in practical simulations of engineering turbulent flows by pure geometrical reasons. An anisotropic grid corresponds to an anisotropic filter which may be used to take into account also of the anisotropy of subgrid turbulence structures. With the intention of a more correct representation of subgrid scales anisotropicity, an anisotropic filter should be associated to an anisotropic subgrid model unhampered by the isotropicity Kolmogorov hypothesis. Some anisotropic models have been developed to the intent to represent the anisotropy of the unresolved scales [3]. The determination of the characteristic length $\overline{\Delta}$ that must be used to compute the subgrid stresses is still an open question when functional models, in particular the eddy viscosity models, are used in anisotropic conditions. Two different approaches, resumed in the follow, can be used to tackle this problem.

The first approach consists in defining a single length scale for representing the filter and is more suitable for scalar eddy viscosity models, although, in theory, it is applicable only for slightly anisotropic grids. It is common practice to use the cubic root of the cell volume [4] as filter cutoff length $\overline{\Delta} = \sqrt[3]{\Delta_1 \Delta_2 \Delta_3}$ when a cartesian grid with moderate anisotropies and unequal size Δ_i in the different directions is used.

Scotti at al.[5] suggest the use of a correction function taking in account the grid aspect ratios for stronger grid anisotropies, but the use of this function is limited to cartesian grids.

Actually, for irregular grids, it is generally difficult to provide an expression for the filter width $\overline{\Delta}$. With this kind of grids, the filter width is often taken equal to the cubic root of the element volume $\overline{\Delta} = \sqrt[3]{\Omega_e}$ (i.e. [6, 7]), or twice the smallest length of an edge of the mesh cells [8].

A different method is proposed by Colosqui and Oberai [9]: they did not imposed a priori the filter cutoff size $\overline{\Delta}$, but derived an expression for the Smagorinsky length scale ($C_S\overline{\Delta}^2$) by an energetic analysis in physical space based on the Kolmogorov's hypothesis of isotropicity of the small turbulent scales. In this analysis, they equated the dissipation for the Smagorinsky model to the exact dissipation, both ensamble averaged and integrated over the element grid. The peculiarity of this method is that not only the characteristic grid size $\sqrt[3]{\Omega_e}$ is taken into account, but also the particular basis functions used in the numerical method. Although it is applicable to completely irregular and anisotropic grids, it should be confined to cases where the assumption of isotropicity of small scales is acceptable.

Other authors [10, 11], using a dynamic isotropic model, computed directly the Smagorinsky length scale ($C_S\overline{\Delta}^2$) without the need to specify the grid filter width $\overline{\Delta}$. This approach is very interesting since it bypasses the problem, but some more investigation should be suitable to check that an explicit filter size definition is not necessary.

The second approach, which better takes into account the anisotropy of the filter, introduces several characteristic length scales in the model. Obviously this approach is not suitable for models based on scalar turbulent viscosity. As regard of it, the first proposal was by Bardina et al.[12, 13]. They proposed the use of a tensorial formulation of the cutoff length taking into account the geometry of the cell. They introduced the tensor

$$\mathcal{I}_{ij} = \frac{1}{\Omega_e} \int_{\Omega_e} x_i x_j d\Omega \tag{2}$$

used in an anisotropic formulation of the deviatoric part of the subgrid stress tensor:

$$\begin{aligned}\tau_{ij}-\frac{1}{3}\tau_{kk} &= C_1\frac{1}{3}\mathcal{I}_{mm}|\overline{S}|\overline{S}_{ij}\\ &+ C_2|\overline{S}|\left(\mathcal{I}_{ik}\overline{S}_{kj}+\mathcal{I}_{jk}\overline{S}_{ki}-\frac{1}{3}\mathcal{I}_{lk}\overline{S}_{kl}\delta_{ij}\right)\\ &+ C_3\frac{|\overline{S}|}{\frac{1}{3}\mathcal{I}_{mm}}\left(\mathcal{I}_{ik}\mathcal{I}_{jl}\overline{S}_{kl}+-\frac{1}{3}\mathcal{I}_{ik}\mathcal{I}_{jl}\overline{S}_{kl}\delta_{ij}\right)\end{aligned} \tag{3}$$

where C_1, C_2, C_3 are constant to be determined. They applied this approach to a grid composed by parallelepipeds in cartesian coordinates for which the tensor $\mathcal{I}$ is reduced to be diagonal

$$\mathcal{I}=\begin{bmatrix}\Delta_1^2 & 0 & 0\\ 0 & \Delta_2^2 & 0\\ 0 & 0 & \Delta_3^2\end{bmatrix}. \tag{4}$$

During the last decade, Discontinuous Galerkin (DG) methods have become increasingly popular for Large Eddy Simulation. The definition of the filter operator $\overline{\cdot}$ in the DG discretization, as demonstrated also by Van der Bos et al.[14], is simply defined as the projection over the numerical solution subspace and the characteristic size of the filter results to depend strongly on the spatial resolution. The approach of Colosqui and Oberai taking into account the form of basis functions, could be applied to DG method too but, as already mentioned, it presents the limit of the hypothesis of isotropicity of the small turbulent scales.

The aim of the present work is the investigation of three different approaches for the evaluation of the filter size for anisotropic and non cartesian grid. These formulations will be used in conjunction with the anisotropic model proposed in [15] and then extended to compressible flows [16], with the purpose to better represent the anisotropicity of the small turbulent scales. In particular an original formulation based on the inertial ellipsoid of the grid element is proposed. For the sake of completeness the whole set of equations, including the adopted LES model and the different approaches to the filter size formulations, are reported in Sections 2 and 3. The performances of presented approaches are evaluated for the simulation of compressible flow in the classical plane channel test case. Moreover for a check in a more complex configuration with separated region, the periodic hill test flow has been simulated and the obtained results are presented and discussed in Section 4.

2. Equations and numerical method

In the present work a numerical code based on a Local Discontinuous Galerkin (LDG) method is used. To this aim, a tessellation $\mathcal{T}_h$ of the computational domain Ω into tethrahedral elements Ω_e is introduced. Then the finite element space $\mathcal{V}_h$ is defined as

$$\mathcal{V}_h=\left\{v_h\in L^2(\Omega): v_h|_{\Omega_e}\in\mathbb{P}^q(\Omega_e),\,\forall K\in\mathcal{T}_h\right\}.$$

$\mathbb{P}^q(\Omega_e)$ denotes the space of polynomial functions of total degree q.

Let $\Pi_{\mathcal{V}} : L^2(\Omega) \to \mathcal{V}$ be the L^2 projector over the subspace $\mathcal{V} \subset L^2(\Omega)$, defined by

$$\int_\Omega \Pi_{\mathcal{V}} \phi \, v \, d\mathbf{x} = \int_\Omega \phi \, v \, d\mathbf{x}, \qquad \forall \phi, v \in \mathcal{V}.$$

The filter $\overline{\cdot}$ is now simply defined as the projection over the finite dimensional numerical solution subspace

$$\overline{\phi} = \Pi_{\mathcal{V}_h} \phi = \phi_h.$$

For this reason the filtered prognostic quantities $\overline{\rho}$, $\overline{\rho \mathbf{u}}$ and $\overline{\rho e}$ can be identified with their numerical solution counterparts ρ_h, $(\rho \mathbf{u})_h$ and $(\rho e)_h$. In this approach, the characteristic size of the filter results to depend strongly on the spatial resolution and on the definition of a characteristic size of the element Ω_e. As customary in compressible LES and RANS, to avoid subgrid terms in the continuity equation, the Favre filter operator $\widetilde{\cdot}$ defined as

$$\widetilde{\phi} = \frac{\overline{\rho \phi}}{\overline{\rho}}$$

is introduced besides the filter in space $\overline{\cdot}$.

To model a turbulent compressible flow in a LES context, the following filtered Navier–Stokes equations, in non dimensional form, are used

$$\partial_t \overline{\rho} + \partial_j (\overline{\rho} \widetilde{u}_j) = 0 \tag{5a}$$

$$\partial_t \left(\overline{\rho} \widetilde{u}_i \right) + \partial_j \left(\overline{\rho} \widetilde{u}_i \widetilde{u}_j \right) = -\frac{1}{\gamma \, Ma^2} \partial_i \overline{p} + \frac{1}{Re} \partial_j \widetilde{\sigma}_{ij} - \partial_j \tau_{ij} + \overline{\rho} f_i \tag{5b}$$

$$\begin{aligned} \partial_t \left(\overline{\rho} \widetilde{e} \right) + \partial_j \left(\overline{\rho} \widetilde{h} \widetilde{u}_j \right) = & \frac{\gamma \, Ma^2}{Re} \partial_j \left(\widetilde{u}_i \widetilde{\sigma}_{ij} \right) - \frac{1}{\kappa Re Pr} \partial_j \widetilde{q}_j \\ & - \frac{1}{\kappa} \partial_j Q_j - \frac{\gamma Ma^2}{2} \partial_j \left(J_j \tau_{kk} \widetilde{u}_j \right) + \gamma Ma^2 \overline{\rho} f_j \widetilde{u}_j. \end{aligned} \tag{5c}$$

Following the approach outlined in [16] in a DG context, the equations have been implicitly filtered in space and the filtered variables are density $\overline{\rho}$, velocity $\tilde{\mathbf{u}}$ and specific total energy $\tilde{e}$.

Here $\overline{p}$ denotes the pressure, $\mathbf{f}$ a prescribed forcing, $\overline{\rho h} = \overline{\rho} \widetilde{h} = \overline{\rho} \widetilde{e} + \overline{p}$ the enthalpy and $\widetilde{\sigma}$ and $\widetilde{\mathbf{q}}$ the momentum and heat diffusive fluxes, respectively. The Mach and Reynolds number are defined as

$$Ma = \frac{V_r}{(\gamma R T_r)^{1/2}}, \qquad Re = \frac{\rho_r V_r L_r}{\mu_r},$$

for which the reference length L_r, density ρ_r, velocity V_r and temperature T_r are assumed. The other non dimensional numbers based on the gas specific heat and ideal gas constant are

$$\gamma = \frac{c_p}{c_v}, \qquad \kappa = \frac{R}{c_p}.$$

Equations (5) must be completed by a state equation

$$\overline{p} = \overline{\rho}\widetilde{T},$$

and by the constitutive equations:

$$\widetilde{\sigma}_{ij} = 2\mu\widetilde{\mathcal{S}}_{ij} - \frac{2}{3}\widetilde{\mathcal{S}}_{kk}\delta_{ij}, \qquad \widetilde{q}_i = -\mu\partial_i\widetilde{T}.$$

where the strain rate tensor is defined as

$$\widetilde{\mathcal{S}}_{ij} = \frac{1}{2}\left(\partial_j\widetilde{u}_i + \partial_i\widetilde{u}_j\right)$$

and the dynamic viscosity is assumed

$$\mu(\widetilde{T}) = \widetilde{T}^{\alpha}$$

according to the Sutherland law. Defining the internal energy $\widetilde{e}_{\mathrm{i}}$ in function of the temperature $\widetilde{T}$:

$$\widetilde{e}_{\mathrm{i}} = \frac{1-\kappa}{\kappa}\widetilde{T}$$

we also get

$$\widetilde{e} = \widetilde{e}_{\mathrm{i}} + \frac{\gamma Ma^2}{2}\widetilde{u}_k\widetilde{u}_k.$$

Following [16] a number of subgrid terms are neglected and only the relevant ones are considered. By this way the contributions to be modelled are the subgrid stress tensor $\tau_{ij} = \overline{\rho u_i u_j} - \overline{\rho}\widetilde{u}_i\widetilde{u}_j$, the subgrid heat flux $Q_i = \overline{\rho u_i T} - \overline{\rho}\widetilde{u}_i\widetilde{T}$ and the turbulent diffusion flux $J_i = \overline{\rho u_i u_k u_k} - \overline{\rho}\widetilde{u}_i\widetilde{u}_k\widetilde{u}_k$.

3. Subgrid anisotropic model

Concerning the subgrid contributions, the anisotropic model proposed in [15] and extended to compressible flows in [16] is used. In this model the subgrid stress tensor τ is assumed to be proportional to the strain rate tensor $\widetilde{\mathcal{S}}$ through a fourth order symmetric tensor

$$\tau_{ij} = -\overline{\rho}\overline{\Delta}^2|\widetilde{\mathcal{S}}|\mathcal{B}_{ijrs}\widetilde{\mathcal{S}}_{rs}. \tag{6}$$

where $|\widetilde{\mathcal{S}}| = \sqrt{2\widetilde{\mathcal{S}}_{ij}\widetilde{\mathcal{S}}_{ij}}$. Using a rotation tensor a_{ij} the tensor $\mathcal{B}_{ijrs}$ can be contracted into a second order symmetric tensor $\mathcal{C}_{\alpha\beta}$:

$$\mathcal{B}_{ijrs} = \sum_{\alpha,\beta=1}^{3} \mathcal{C}_{\alpha\beta}a_{i\alpha}a_{j\beta}a_{r\alpha}a_{s\beta},$$

where the components $\mathcal{C}_{\alpha\beta}$ are to be computed with the Germano dynamic procedure [17]. The tensor a_{ij} can in principle be any rotation tensor, possibly varying in space and time.

The dynamic computation of the components $\mathcal{C}_{\alpha\beta}$ relies on the introduction of a test filter operator $\widehat{\cdot}$. To define the test filter, we then introduce

$$\widehat{\mathcal{V}}_h = \left\{ v_h \in L^2(\Omega) : v_h|_{\Omega_e} \in \mathbb{P}^{\widehat{q}}(\Omega_e),\ \forall \Omega_e \in \mathcal{T}_h \right\},$$

where $0 \leq \widehat{q} < q$, and we let, for $v \in L^2(\Omega)$,

$$\widehat{v} = \Pi_{\widehat{\mathcal{V}}_h} v.$$

The test filter is also associated to a Favre filter, denoted by $\breve{\cdot}$, through the Favre decomposition

$$\widehat{\rho\phi} = \widehat{\rho}\breve{\phi}.$$

The application of the dynamic procedure, as described in details in [16], provides the expression for the components of the tensor $\mathcal{C}$

$$\mathcal{C}_{\alpha\beta} = \frac{a_{i\alpha}\mathcal{L}_{ij}a_{j\beta}}{a_{r\alpha}a_{s\beta}\left(\widehat{\overline{\rho}\overline{\Delta}^2|\widetilde{\mathcal{S}}|\widetilde{\mathcal{S}}_{rs}} - \widehat{\overline{\rho}}\widehat{\Delta}^2|\breve{\widetilde{\mathcal{S}}}|\breve{\widetilde{\mathcal{S}}}_{rs}\right)}$$

where $\mathcal{L}_{ij} = \widehat{\overline{\rho}\widetilde{u}_i\widetilde{u}_j} - \widehat{\overline{\rho}}\breve{\widetilde{u}}_i\breve{\widetilde{u}}_j$ is the Leonard stress tensor. The coefficients $\mathcal{C}_{\alpha\beta}$ are averaged over each element and a clipping is introduced to ensure positive total dissipation.

Similarly, the subgrid heat flux is modelled

$$Q_i = -\overline{\rho}\overline{\Delta}^2|\widetilde{\mathcal{S}}|\mathcal{B}^Q_{ir}\partial_r\widetilde{T}, \tag{7}$$

assuming a symmetric tensor $\mathcal{B}^Q_{ir}$ which is diagonal in the reference defined by the rotation tensor a

$$\mathcal{B}^Q_{ir} = \sum_{\alpha=1}^{3} \mathcal{C}^Q_\alpha a_{i\alpha}a_{r\alpha}.$$

The three coefficients $\mathcal{C}^Q_\alpha$ can be also determined using the dynamic procedure yielding

$$\mathcal{C}^Q_\alpha = \frac{a_{i\alpha}\mathcal{L}^Q_i}{a_{r\alpha}\left(\widehat{\overline{\rho}\overline{\Delta}^2|\widetilde{\mathcal{S}}|\partial_r\widetilde{T}} - \widehat{\overline{\rho}}\widehat{\Delta}^2|\breve{\widetilde{\mathcal{S}}}|\partial_r\breve{\widetilde{T}}\right)}$$

where $\mathcal{L}^Q_i = \widehat{\overline{\rho}\widetilde{u}_i\widetilde{T}} - \widehat{\overline{\rho}}\breve{\widetilde{u}}_i\breve{\widetilde{T}}$.

The anisotropic dynamic procedure is also applied to model the subgrid kinetic energy flux

$$J_i = -\overline{\rho}\overline{\Delta}^2|\widetilde{\mathcal{S}}|\mathcal{B}^J_{ir}\partial_r\left(\frac{1}{2}\widetilde{u}_k\widetilde{u}_k\right) \tag{8}$$

where the symmetric tensor $\mathcal{B}_{ir}^J$ is defined

$$\mathcal{B}_{ir}^J = \sum_{\alpha=1}^{3} \mathcal{C}_\alpha^J a_{i\alpha} a_{r\alpha}.$$

The application of the dynamic procedure yields

$$\mathcal{C}_\alpha^J = a_{i\alpha} \mathcal{L}_i^J / \mathcal{M}_\alpha,$$

where

$$\mathcal{M}_\alpha = a_{r\alpha} \left(\overline{\rho} \overline{\Delta}^2 |\widetilde{\mathcal{S}}| \widehat{\partial_r \left(\frac{1}{2} \widetilde{u}_k \widetilde{u}_k \right)} - \widehat{\overline{\rho}} \widehat{\Delta}^2 |\breve{\widetilde{\mathcal{S}}}| \partial_r \left(\frac{1}{2} \breve{\widetilde{u}}_k \breve{\widetilde{u}}_k \right) \right)$$

and $\mathcal{L}_i^J = \widehat{\overline{\rho} \widetilde{u}_i \widetilde{u}_k} \widetilde{u}_k - \widehat{\overline{\rho}} \breve{\widetilde{u}}_i \breve{\widetilde{u}}_k \breve{\widetilde{u}}_k$ is the kinetic energy Leonard flux.

In the following this anisotropic model is proposed combined with different approaches for the definition of the filter size $\overline{\Delta}$ and different rotation tensor a_{ij}. For sake of clarity, the version utilized by Abbà et al. in [16] is reported in the Section 3.1.

3.1. *Anisotropic model using cubic root of element volume*

In previous applications [16] the basis of the orthogonal cartesian reference system has been choose as rotation tensor a so $a_{ij} = \delta_{ij}$ and the subgrid contributions have been modelled as

$$\tau_{ij} = -\overline{\rho} \overline{\Delta}^2 \mathcal{C}_{ij} |\widetilde{\mathcal{S}}| \widetilde{\mathcal{S}}_{ij} \tag{9a}$$

$$Q_i = -\overline{\rho} \overline{\Delta}^2 \mathcal{C}_i^Q |\widetilde{\mathcal{S}}| \partial_i \widetilde{T} \tag{9b}$$

$$J_i = -\overline{\rho} \overline{\Delta}^2 |\widetilde{\mathcal{S}}| \mathcal{C}_i^J \partial_i \left(\frac{1}{2} \widetilde{u}_k \widetilde{u}_k \right). \tag{9c}$$

The filter scales $\overline{\Delta}$ and $\widehat{\Delta}$ are defined as piecewise constant values on each element and are estimated as suggested by Scotti et al. [5] for strongly anisotropic meshes. For each tetrahedral element K, we first denote by $\Delta^{(i)}(K)$ the dimensions of the hexahedron from which the element is obtained, for $i = x, y, z$. Then, for each element K, we define

$$a_l = \frac{\Delta^{(l)}(K)}{\max_i \Delta^{(i)}(K)} \qquad a_k = \frac{\Delta^{(k)}(K)}{\max_i \Delta^{(i)}(K)}$$

where l and k are the directions in which the maximum is not attained, and

$$f = \cosh \sqrt{\frac{4}{27} \left[(\ln a_l)^2 - \ln a_l \ln a_k + (\ln a_k)^2 \right]}$$

$$\overline{\Delta}(K) = \left(\frac{\prod_{i=1}^3 \Delta^{(i)}(K)}{N_q} \right)^{1/3} f.$$

where, using fourth order polynomial degree, $N_q = 35$. The test filter scale $\widehat{\Delta}(K)$ is defined analogously, considering that the polynomial degree for $\widehat{\mathcal{V}}_h$ is $\widehat{q} = 2$, resulting in $N_{\widehat{q}} = 10$ degrees of freedom in each element.

In the following this formulation will be referred as version A1 model.

3.2. *Anisotropic model using an equivalent Smagorinsky length scale*

In previous works [10][11], the filter size $\overline{\Delta}$ has not been *a priori* defined but an equivalent Smagorinsky length scale ($\mathcal{C}\overline{\Delta}^2$) has been computed dynamically using the Germano identity. This approach could be particularly advantageous using unstructured grids. In [10][11] the cited equivalent Smagorinsky length scale has been used in the eddy viscosity dynamic model for the subgrid stresses and heat flux. In the present work this approach is applied to model all the subgrid terms with the anisotropic formulation illustrated in Section 3.1. By this way we get:

$$\begin{aligned}
\tau_{ij} &= -\overline{\rho}\mathcal{C}'_{ij}|\widetilde{\mathcal{S}}|\widetilde{\mathcal{S}}_{ij} \\
Q_i &= -\overline{\rho}\mathcal{C}'^{Q}_{i}|\widetilde{\mathcal{S}}|\partial_i\widetilde{T} \\
J_i &= -\overline{\rho}\mathcal{C}'^{J}_{i}|\widetilde{\mathcal{S}}|\partial_i\left(\frac{1}{2}\widetilde{u}_k\widetilde{u}_k\right)
\end{aligned}$$

where

$$\mathcal{C}'_{ij} = \overline{\Delta}^2\mathcal{C}_{ij}, \qquad \mathcal{C}'^{Q}_{i} = \overline{\Delta}^2\mathcal{C}^{Q}_{i}, \qquad \mathcal{C}'^{J}_{i} = \overline{\Delta}^2\mathcal{C}^{J}_{i}.$$

The Germano identity can be here expressed by

$$\begin{aligned}
\mathcal{L}_{ij} &= \mathcal{C}'_{ij}\left(\widehat{\overline{\rho}|\widetilde{\mathcal{S}}|\widetilde{\mathcal{S}}_{rs}} - \widehat{\overline{\rho}}\left(\frac{\widehat{\Delta}}{\overline{\Delta}}\right)^2|\breve{\widetilde{\mathcal{S}}}|\breve{\widetilde{\mathcal{S}}}_{rs}\right) \\
\mathcal{L}^{Q}_{i} &= \mathcal{C}'^{Q}_{i}\left(\widehat{\overline{\rho}|\widetilde{\mathcal{S}}|\partial_r\widetilde{T}} - \widehat{\overline{\rho}}\left(\frac{\widehat{\Delta}}{\overline{\Delta}}\right)^2|\breve{\widetilde{\mathcal{S}}}|\partial_r\breve{\widetilde{T}}\right) \\
\mathcal{L}^{J}_{i} &= \mathcal{C}'^{J}_{i}\left(\widehat{\overline{\rho}|\widetilde{\mathcal{S}}|\partial_r\left(\frac{1}{2}\widetilde{u}_k\widetilde{u}_k\right)} - \widehat{\overline{\rho}}\left(\frac{\widehat{\Delta}}{\overline{\Delta}}\right)^2|\breve{\widetilde{\mathcal{S}}}|\partial_r\left(\frac{1}{2}\breve{\widetilde{u}}_k\breve{\widetilde{u}}_k\right)\right).
\end{aligned} \tag{12a}$$

where the ratio $(\widehat{\Delta}/\overline{\Delta})^2 = (N_q/N_{\widehat{q}})^2$ is constant. Then the equivalent Smagorinsky lengths are, as usual, determined with the dynamic procedure.

In the following this formulation will be referred as version A2 model.

3.3. *Anisotropic model using the inertial tensor of the grid element*

To take into account of the anisotropy and orientation of the element of the computational domain, the ellipsoid of the inertia tensor of the cell is considered. The semiaxis of the ellipsoid are equal to the reciprocal of the square root of the corresponding principal inertial momentum. The length of the semiaxis is larger in the direction of elongation of a non symmetric grid, so the ellipsoid can well represent the anisotropy

of the cell element and the typical length scale related to a filter in the different directions. This approach appears particularly interesting if the rotation tensor a of the anisotropic dynamic model is associated to the principal axis of inertia of the element. So, once the components of the inertial tensor normalized by the volume of the grid element

$$\mathcal{I}_{ij} = \frac{1}{\Omega_e} \int_{\Omega_e} \left[2(\xi_i - \xi_{i_G})(\xi_j - \xi_{j_G})\delta_{ij} - (\xi_i - \xi_{i_G})(\xi_j - \xi_{j_G}) \right] d\Omega \tag{13}$$

are computed, its eigenvalues λ_i and eigenvectors $\boldsymbol{\omega}_i$, $i = 1, 2, 3$, can be determined using the relations

$$\det|\mathcal{I} - \lambda I| = 0, \qquad \lambda\mathcal{I} = \boldsymbol{\omega} I$$

where I is the identity matrix. In the equation (13) G denotes the barycentre of the grid element.

In the equations (6), (7), (8) the scalar $\overline{\Delta}^2$ is substituted by a tensor $\overline{\Lambda}$ of elements

$$\overline{\Lambda}_{ij} = \frac{1}{\sqrt{\lambda_i \lambda_j}} \frac{1}{N_q^2}$$

and similarly the test filter scale $\widehat{\Delta}^2$ is substituted by

$$\widehat{\Lambda}_{ij} = \frac{1}{\sqrt{\lambda_i \lambda_j}} \frac{1}{N_{\widehat{q}}},$$

while the a_{ij} elements of the rotation matrix are assumed equal to the $i-$th component of the $\boldsymbol{\omega}_j$ eigenvector. Thus the subgrid stress tensor results

$$\tau_{ij} = -\overline{\rho}|\widetilde{\mathcal{S}}| \sum_{\alpha,\beta=1}^{3} \mathcal{C}_{\alpha\beta} \overline{\Lambda}_{\alpha\beta} a_{i\alpha} a_{j\beta} a_{r\alpha} a_{s\beta} \widetilde{\mathcal{S}}_{rs}$$

and the coefficients are determined by the relations

$$\mathcal{C}_{\alpha\beta} = \frac{a_{i\alpha} \mathcal{L}_{ij} a_{j\beta}}{a_{r\alpha} a_{s\beta} \left(\widehat{\overline{\rho}\overline{\Lambda}_{\alpha\beta}|\widetilde{\mathcal{S}}|} \widetilde{\mathcal{S}}_{rs} - \widehat{\overline{\rho}} \widehat{\Lambda}_{\alpha\beta} |\breve{\widetilde{\mathcal{S}}}| \breve{\widetilde{\mathcal{S}}}_{rs} \right)}$$

where the summation over α and β is suppressed.

Similarly, the subgrid heat flux is modelled as:

$$Q_i = -\overline{\rho}|\widetilde{\mathcal{S}}| \sum_{\alpha=1}^{3} \mathcal{C}_{\alpha}^{Q} \overline{\Lambda}_{\alpha\alpha} a_{i\alpha} a_{r\alpha} \partial_r \widetilde{T},$$

$$\mathcal{C}_{\alpha}^{Q} = \frac{a_{i\alpha} \mathcal{L}_i^Q}{a_{r\alpha} \left(\widehat{\overline{\rho}\overline{\Lambda}_{\alpha\alpha}|\widetilde{\mathcal{S}}|} \partial_r \widetilde{T} - \widehat{\overline{\rho}} \widehat{\Lambda}_{\alpha\alpha} |\breve{\widetilde{\mathcal{S}}}| \partial_r \breve{\widetilde{T}} \right)},$$

and, coherently with the other subgrid contributions, the subgrid kinetic energy flux

$$J_i = -\overline{\rho}|\widetilde{\mathcal{S}}| \sum_{\alpha=1}^{3} \mathcal{C}_\alpha^J \overline{\Lambda}_{\alpha\alpha} a_{i\alpha} a_{r\alpha} \partial_r \left(\frac{1}{2} \widetilde{u}_k \widetilde{u}_k \right)$$

$$\mathcal{C}_\alpha^J = a_{i\alpha} \mathcal{L}_i^J / \mathcal{M}_\alpha,$$

where

$$\mathcal{M}_\alpha = a_{r\alpha} \left(\overline{\rho}\overline{\Lambda}_{\alpha\alpha} \widetilde{|\mathcal{S}|\partial_r \left(\frac{1}{2} \widetilde{u}_k \widetilde{u}_k \right)} - \widehat{\overline{\rho}}\widehat{\Lambda}_{\alpha\alpha} \breve{\widetilde{|\mathcal{S}|}} \partial_r \left(\frac{1}{2} \breve{\widetilde{u}}_k \breve{\widetilde{u}}_k \right) \right).$$

In the following this formulation will be referred as version A3 model.

4. Numerical results

4.1. *Plane channel flow simulations*

In order to compare the performances of the described approaches, we have computed a typical LES benchmark for compressible, periodic, plane channel flow. The results obtained with the A2 and A3 versions are compared here with the data from the direct numerical simulation (DNS) of Wei and Pollard [18] and with the results obtained with the A1 one in a previous work [16].

All the computations were performed using the `FEMilaro` finite element library [19], a FORTRAN/MPI library which is publicly available under GPL license.

The computational domain Ω is a box of size $L_x/h = 4\pi$, $L_y/h = 2$, $L_z/h = 2\pi$ in dimensionless units, and it is aligned with a reference frame such that x represents the streamwise axis, y the wall normal and z the spanwise axis. The bulk Reynolds number $Re_\mathrm{b} = 2795$ and Mach number $Ma_\mathrm{b} = 0.7$, defined as

$$Re_\mathrm{b} = \frac{\rho_\mathrm{b} U_\mathrm{b} h}{\mu_\mathrm{w}}, \qquad Ma_\mathrm{b} = \frac{U_\mathrm{b}}{\sqrt{\gamma R T_\mathrm{w}}},$$

are imposed. Here h is the half height of the channel, ρ_b and U_b are the bulk density and the bulk velocity, respectively, T_w is the wall temperature and $\mu_\mathrm{w} = \mu(T_\mathrm{w})$ is the viscosity of the fluid at the wall.

Isothermal, no-slip boundary conditions are imposed at the walls for $y/h = \pm 1$, while periodic conditions are applied in the streamwise and spanwise directions. The simulations are initialised with a random noise superimposed to a parabolic velocity profile in the streamwise direction, and uniform density and temperature fields. A uniform in space body force is included along the streamwise direction in order to guarantie the flow rate corresponding to the desired bulk velocity. The wall shear stress τ_w, the friction Reynolds number Re_τ and the skin friction velocity u_τ, defined as

$$\tau_\mathrm{w} = \mu_\mathrm{w} (\partial_y < u_x >)_\mathrm{w}, \quad Re_\tau = \sqrt{\rho_\mathrm{w} Re_\mathrm{b} \frac{\tau_\mathrm{w}}{\mu_\mathrm{w}}},$$

Table 1. Parameters of the LES simulations and reference DNS [18].

	L_x	L_z	Δ_x^+	Δ_z^+	$\Delta_{y_{min}}^+/\Delta_{y_{max}}^+$
DNS	12	6	4.89	4.89	0.19/2.89
Presents	4π	$\frac{4}{3}\pi$	24	11	0.67/8.2

Table 2. Mean flow quantities obtained by the numerical simulations of the plane channel flow at $Re_b = 2795$ and $Ma_b = 0.7$. The results obtained using the subgrid models proposed in Section 3 are compared with the reference DNS [18].

	$\tau_{\rm w}$	Re_τ	$u_\tau/U_{\rm b}$	$\rho_{\rm w}/\rho_{\rm b}$	$U_{\rm c}/U_{\rm b}$	$\rho_{\rm c}/\rho_{\rm b}$	$\rho_{\rm c}/\rho_{\rm w}$	$T_{\rm c}/T_{\rm w}$
DNS	12.38	186	0.0618	1.107	1.16	0.995	0.925	1.086
A1	10.31	176	0.0588	1.063	1.15	0.997	0.938	1.069
A2	10.4	176	0.059	1.068	1.15	0.996	0.932	1.076
A3	11.16	177	0.0631	1.064	1.15	0.996	0.936	1.071

$$u_\tau = \frac{Re_\tau}{Re_{\rm b}\rho_{\rm w}}$$

are computed *a posteriori* for each simulation.

The computational mesh is obtained by a structured mesh with $N_x = 16$, $N_y = 16$, $N_z = 12$ hexahedra in the x, y, z directions, respectively, each of which is then split into $N_t = 6$ tetrahedral elements. While uniform in the x, z directions, the hexahedral mesh is stretched in the y direction by a hyperbolic tangent law in order to ensure a sufficient resolution of the boundary layer. The polynomial degree for $\mathcal{V}_h$ is $q = 4$, resulting in $N_q = 35$ degrees of freedom in each element. Hence, we can define an equivalent grid spacing

$$\Delta_{x,z} = \frac{L_{x,z}}{N_{x,z}\sqrt[3]{N_t N_q}} \qquad \Delta_{y_i} = \frac{y_i - y_{i-1}}{\sqrt[3]{N_t N_q}},$$

and, in wall units, $\Delta_i^+ = Re_\tau \Delta_i$, for $i = x, y, z$. Using the skin friction Reynolds number of the corresponding DNS, we can now determine $\Delta_{y_1} = \Delta_{y_{min}} = Re_\tau^{-1}\Delta_{y_{min}}^+$ requiring that several points are located at a distance from the wall $y^+ < 5$, so that the boundary layer is well resolved. The grid parameters are summarized in Table 1.

After the statistical steady state was reached, the simulations were continued for a dimensionless time equal to 90 in order to verify time invariance of the mean profiles and to compute all the statistics. In the following $< \cdot >$ means average in time and in the homogeneous directions.

The A3 version requires about 10% of computational time more than the other two versions.

In Table 2, the mean flow quantities at the wall and at the channel centreline, denoted respectively by the subscripts w and c, are compared with the reference DNS results.

Since during the simulations a constant mass flow is imposed, the wall shear stress $\tau_{\rm w}$ can differ from the expected DNS value. Table 2 demonstrates that the prediction of the wall stress is extremely sensitive to the used approach. The relative errors for the wall stress and the friction velocity range, respectively, between $9 \div 17\%$ and $2 \div 5\%$, where the larger values are obtained with A1. The Reynolds number Re_τ and the friction velocity u_τ are affected by the wall shear stress error and by the fact that the

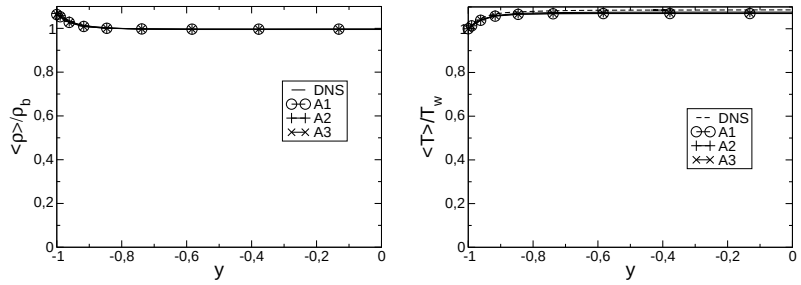

(a) Mean density normalized by the bulk density.

(b) Mean temperature normalized by the wall temperature.

Figure 1. Mean density and temperature profiles in the plane channel flow at $Re_b = 2795$ and $Ma_b = 0.7$.

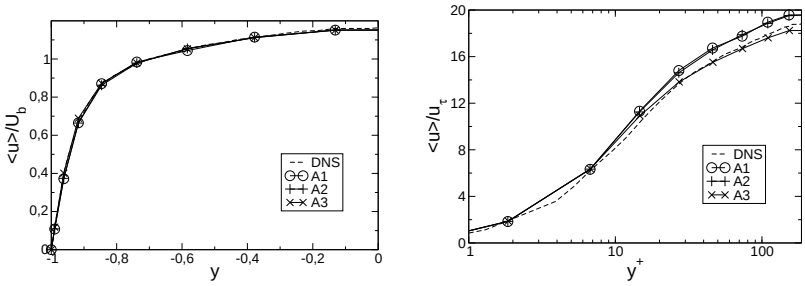

(a) (b)

Figure 2. Mean streamwise velocity profile in the channel flow at $Re_b = 2795$ and $Ma_b = 0.7$. (a): in bulk units; (b): in wall units.

density ρ_{w} at the wall is underpredicted. On the contrary, at the centre of the channel density values are a bit higher than the reference ones and, coherently, temperature values are lower. In any cases, the discrepances between the DNS and the present simulations are less then 4% for the density and 2% for the temperature and the three considered versions A1, A2 and A3 perform in a similar manner.

Figure 1 shows the mean profiles. The shape of the mean density and temperature are coherent with the values of Table 2.

In Figure 2 the mean streamwise velocity profiles are represented. The differences between the mean velocity profiles obtained with the different versions of the anisotropic model are evident when plotted in wall units. The model version A3 better reproduces the correct slope of the mean velocity at the wall, consistent with the higher wall stress τ_w, so the intercepts of the logarithmic layer is well captured and the mean velocity profile well reproduces the DNS one. Looking at the mean quantities, we can conclude that the version A3 based on the eigenvectors and eigenvalues of the inertial matrix of the grid element, performs globally better.

In Figure 3, the profiles of the mean total, modelled $< \tau_{ij} >$ plus resolved $< \overline{\rho} >< u_i' u_j' >$, turbulent stresses are displayed. Here $u_i' = \tilde{u}_i - < \tilde{u}_i >$ are the resolved fluctuations. The fluctuations of the normal to the wall and spanwise velocity components are underestimated by both version A1 and A2. It can be observed that the DNS results are very well reproduced by the version A3 model. Relevant differences also affect the wall normal turbulent shear stress (modelled + resolved) reported

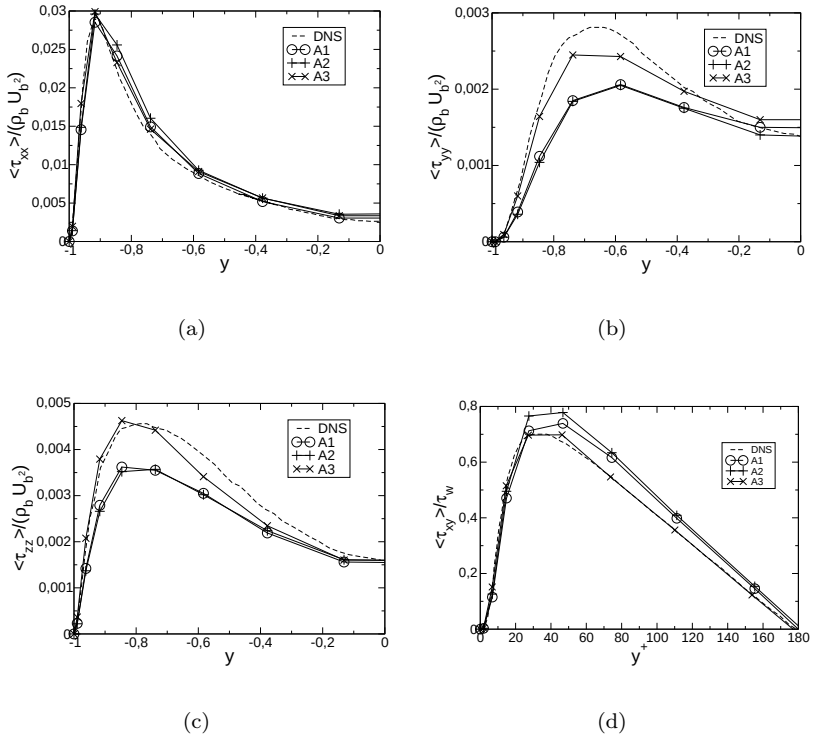

Figure 3. Profiles of the mean total (resolved plus modelled) turbulent stresses in the plane channel flow at $Re_b = 2795$ and $Ma = 0.7$. (a): normal component in streamwise direction $(< \tau_{xx} > + < \rho >< u'_x u'_x >)/(\rho_b U_b^2)$; (b): $(< \tau_{yy} > + < \rho >< u'_y u'_y >)/(\rho_b U_b^2)$; (c): $(< \tau_{zz} > + < \rho >< u'_z u'_z >)/(\rho_b U_b^2)$; (d): $(< \tau_{xy} > + < \rho >< u'_x u'_x >)/\tau_w$ in wall units.

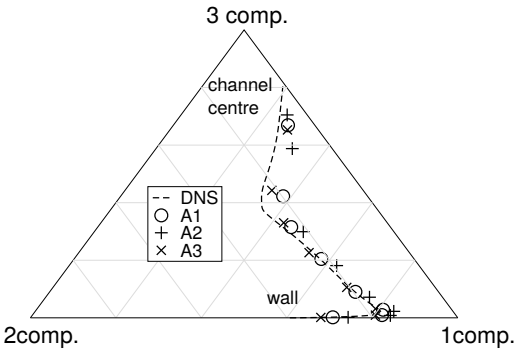

Figure 4. Barycentric map [20]. The anisotropy of the total, modelled plus resolved, turbulent stress tensor from present LES are compared with the Reynolds stress tensor from the reference DNS.

in Figure 3(d).

The good behaviour of the A3 formulation is also confirmed by the turbulence barycentric map in Figure 4 which quantifies the anisotropy of the Reynolds stress tensor [20]. In this map the eingenvalues of the total turbulent stress anisotropy tensor

$$\alpha_{ij} = \frac{\tau_{ij} + < \rho >< u_i' u_j' >}{\tau_{kk} + < \rho >< u_k' u_k' >} - \frac{\delta_{ij}}{3} \tag{14}$$

obtained by the present numerical experiments are compared with the Reynolds stress anisotropy tensor from the reference DNS. The version A3 presents a behaviour very similar to the DNS one not only in the wall region, where the turbulence is strongly anisotropic and the one component limiting state of turbulence is dominant, but also far from the wall. Actually, as demonstrated by Banerjee et al.[20], the turbulence in the centre of the channel is far from isotropy although the limiting three components state is dominant,making the anisotropic character of the subgrid scale model important also in this region. The version A2 performs worst showing a trend more axisymmetric then the DNS.

Finally we can conclude that not only the use of the subgrid model not subjected to small scales isotropicity assumption, as the anisotropic model used in the present work, is important in LES of non homogeneous turbulent flows, but also the definition of a filter size taking into account the anisotropicity of the numerical grid, as in version A3, play an important role.

4.2. *Flow over periodic hills*

Turbulent flow over a periodic hill has been simulated to evaluate the performance of the proposed subgrid scale model formulations in a more complex configuration, in which separation and reattachment arise and a less trivial geometry is considered. First studied in [21], the periodic hill flow has become an important test case for turbulent flow simulation [22–24]. In fact the periodic hill test case presents some challenging feature, like the massive flow separation from a curved surface, a reattachment and a strong acceleration. The results obtained with the A2 and A3 versions are in the following compared with those obtained using the A1 one in a previous work [16] and

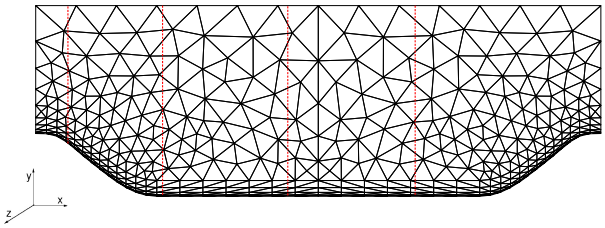

Figure 5. Periodic hill geometry and section in the $(x-y)$ plane of the mesh used for the periodic hill simulations; the dashed lines at $x/h = 0.5, 2, 4, 6$ denote the positions of the mean profiles displayed in the following figures.

with the results obtained by Breuer et al. [22] in an incompressible direct numerical simulation.

The computational domain (Fig. 5) is a periodic plane channel constricted by a hill of height h about one third of the total channel height. Domain has nondimensional size $L_x/h = 9.0$ in the streamwise direction, $L_z/h = 4.5$ in the spanwise direction and $L_y/h = 3.036$ in the height. A structured hexahedral mesh, where each hexahedron is divided into 6 tetrahedra, is used in the layer close to the lower wall, while a fully unstructured, three-dimensional mesh is used in the bulk region. A side section of the resulting mesh is shown in Figure 5. The total number of elements is 16662. In the wall boundary layer $N_z = 12$ elements in the spanwise direction are used, which, using basis functions of degree $q = 4$, leads to a $\Delta z \simeq 0.062$. The streamwise resolution varies from $\Delta x \simeq 0.062$ between the two hills to $\Delta x \simeq 0.023$ at the top of the hill. The mesh is refined in the normal direction to reach $\Delta y \simeq 0.0032$ at the bottom wall. No mesh refinement has been applied close to the upper wall where a free slip isothermal boundary condition is imposed. The no-slip and isothermal wall boundary conditions are imposed at the lower surface while cyclic boundary conditions are imposed in the streamwise and spanwise directions where the flow is assumed to be periodic. As in the channel flow simulation, a varying in time driving force is applied to keep constant mass flow. The bulk Reynolds and Mach numbers, defined as

$$Re_{\mathrm{b}} = \frac{\rho_{\mathrm{b}} U_{\mathrm{b}} h}{\mu_{\mathrm{w}}}, \qquad Ma_{\mathrm{b}} = \frac{U_{\mathrm{b}}}{\sqrt{\gamma R T_{\mathrm{w}}}}, \tag{15}$$

are imposed, where U_{b} and ρ_{b} are respectively the bulk velocity and density evaluated on the crest of the hill, and T_{w} and μ_{w} are the temperature and the viscosity at the wall. The values we have employed are $Re_{\mathrm{b}} = 2800$ and $Ma_{\mathrm{b}} = 0.2$.

In Figure 6 the profiles located at $x/h = 0.5$, just after the separation and through the strong shear layer, don't present any relevant differences between the results of the three proposed versions: the mean velocity gradient at the wall, the peak value and the position of the turbulent stresses very well reproduce the DNS profiles. This means that the boundary layer and the detachement from the curved wall are well captured.

In Figure 7 the mean profiles at $x = 2$, located at the beginning of the flat floor, inside the main recirculating bubble, are depicted. Regarding the mean streamwise velocity, all the three model versions are in good agreement with the DNS representing the mean back flow. Some differences are present for the other quantities: the A1 version underestimates the normal mean velocity and overestimates the absolute values of the stress components. The turbulent stresses by A2 and A3 are in agreement with the DNS that means the developing free shear layer is well reproduced.

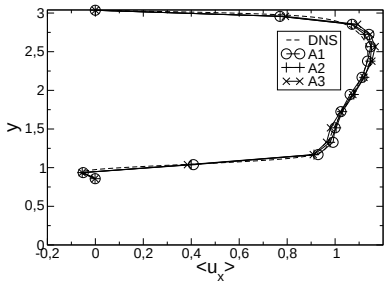

(a) mean streamwise velocity

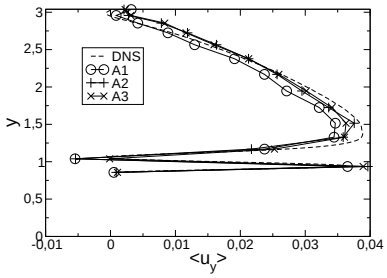

(b) mean normal velocity

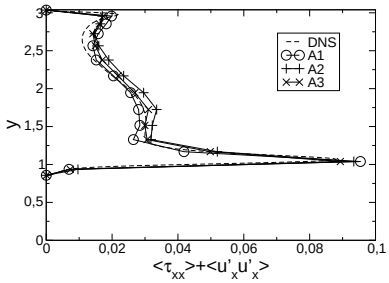

(c) $< \tau_{xx} > + < u'_x u'_x >$

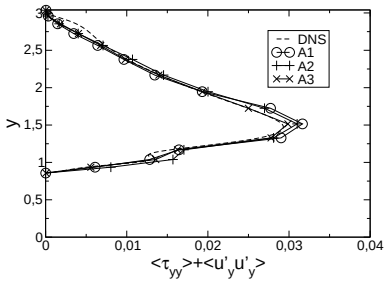

(d) $< \tau_{yy} > + < u'_y u'_y >$

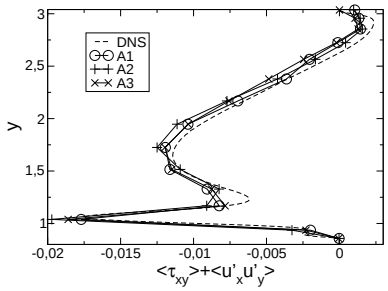

(e) $< \tau_{xy} > + < u'_z u'_y >$

Figure 6. Profiles of mean velocity and total turbulent stresses in the periodic hill flow test case at $x = 0.5$.

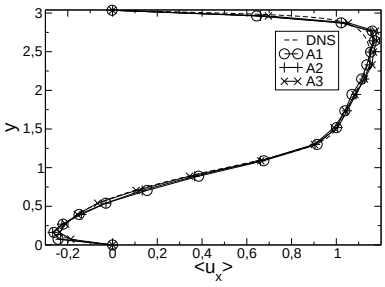

(a) mean streamwise velocity

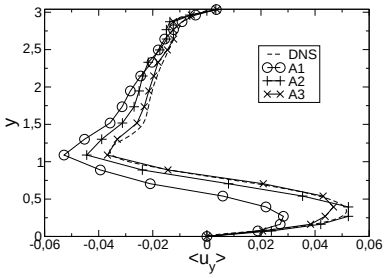

(b) mean normal velocity

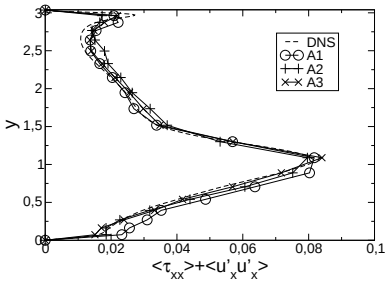

(c) $< \tau_{xx} > + < u'_x u'_x >$

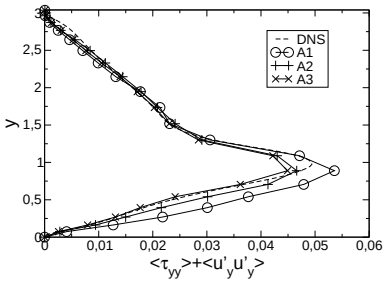

(d) $< \tau_{yy} > + < u'_y u'_y >$

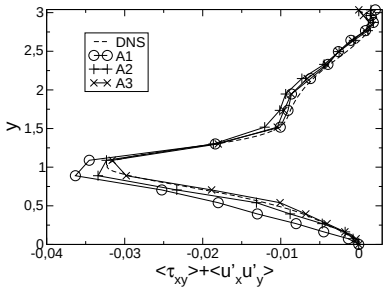

(e) $< \tau_{xy} > + < u'_z u'_y >$

Figure 7. Profiles of mean velocity and total turbulent stresses in the periodic hill flow test case at $x = 2$.

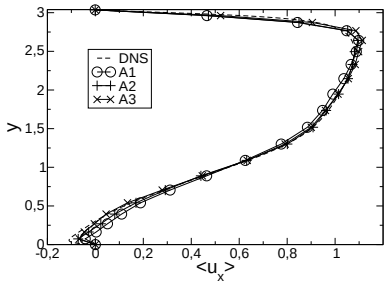

(a) mean streamwise velocity

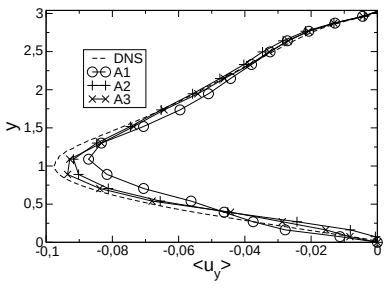

(b) mean normal velocity

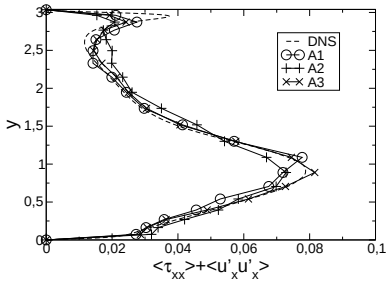

(c) $< \tau_{xx} > + < u'_x u'_x >$

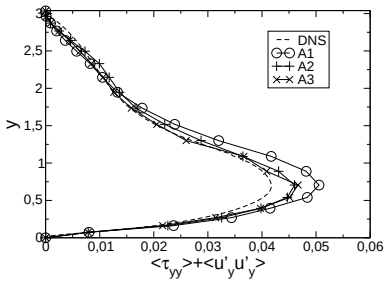

(d) $< \tau_{yy} > + < u'_y u'_y >$

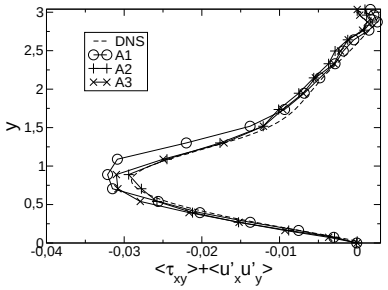

(e) $< \tau_{xy} > + < u'_z u'_y >$

Figure 8. Profiles of mean velocity and total turbulent stresses in the periodic hill flow test case at $x = 4$.

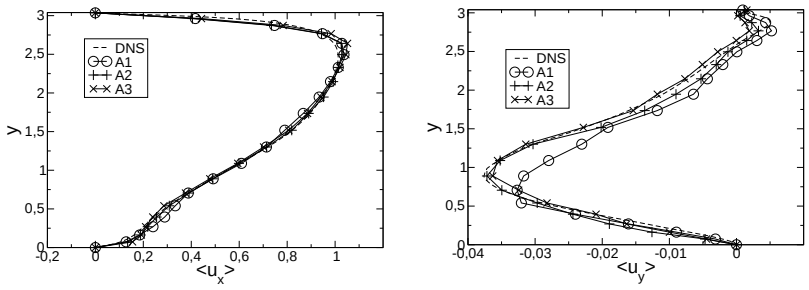

(a) mean streamwise velocity

(b) mean normal velocity

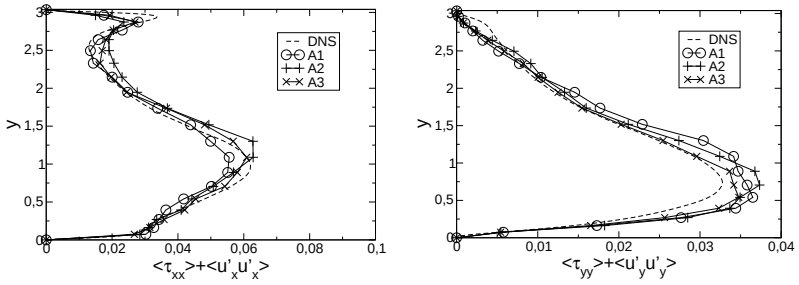

(c) $< \tau_{xx} > + < u'_x u'_x >$

(d) $< \tau_{yy} > + < u'_y u'_y >$

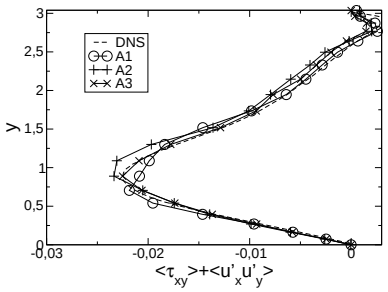

(e) $< \tau_{xy} > + < u'_z u'_y >$

Figure 9. Profiles of mean velocity and total turbulent stresses in the periodic hill flow test case at $x = 6$.

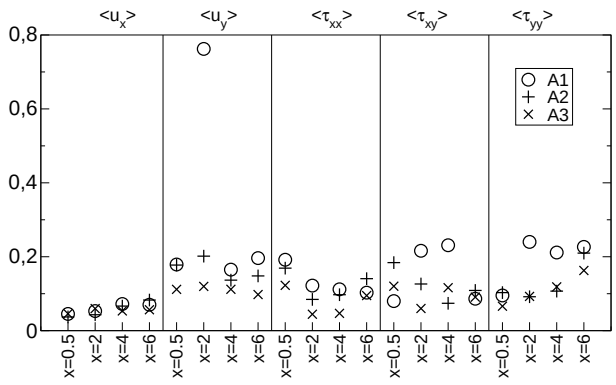

Figure 10. Maximum errors evaluated respect to the reference DNS for the mean profiles represented in Figures 6-9 at different x positions.

Also observing the profiles located close to the end of the recirculating bubble at $x = 4$ (Figure 8), and in the reattached region at $x = 6$ (Figure 9), we can affirm that the A1 version performs worst while A2 and A3 perform in a quite similar manner.

In order to get more quantitative evaluation of the performances, an error for the mean profiles represented in Figures 6-9 has been evaluated: for each mean quantity $\phi(y)$ at a fixed x, the maximum error respect to the DNS is computed as

$$err_\phi = \frac{max(\sqrt{(\phi(y) - \phi_{DNS}(y))^2}}{\max(\sqrt{\phi^2_{DNS}(y)})}$$

and the corresponding values are collected in Figure 10. Looking at this figure, while for the streamwise velocity there are not relevant differences, observing the other components it is evident that the higher errors are obtained with the A1 version. The differences between the A2 and A3 version are lower but the A3 performs globally better. In conclusion, also for this test case, we can appreciate the benefit of using the anisotropic filter size based on the inertial ellipsoid of element grid.

5. Conclusions

We have investigated the potential benefits resulting from the application of different approaches to the definition of the characteristic filter size in the context of the anisotropic dynamic model for LES [15] applied in a numerical code based on high order DG method for compressible flow. The approach in which the Smagorinsky length scale is dynamically computed, and any filter size is not imposed a priori, is here applied to the anisotropic model. Moreover an original approach in which an anisotropic filter size, based on the inertial ellipsoid of the element grid, is here proposed. The results have been compared also to the data obtained using an isotropic filter size defined as the cubic root of the element volume with a correction for anisotropic grids.

A comparison with the DNS experiment results reported in [18] for a compressible flow at Mach number 0.7 in a plane channel shows a clear improvement in the prediction of several key features of the flow when the anisotropic filter size is used. In particular, the mean velocity and turbulent stresses are in very good agreement with the reference DNS, and their anisotropicity is very well reproduced using the tensorial filter size.

The differences between the different approaches are less evident looking at the results obtained by the simulation of a channel flow constricted by periodic hills [22] at Mach number 0.2. In any case it is possible to affirm that the model using the filter size based on the cubic root of the element volume performs worst, do not well reproduce the mean quantities in the shear layer region, and gives the higher errors values. Also in this case the model using the tensorial filter size performs globally better and gets lower errors.

In conclusion the obtained results highlight the importance to use a tensorial filter size in order to take explicitly into account the anisotropy of the grid and to improve the performances of an anisotropic subgrid model.

Acknowledgements

We would like to thank M. Breuer and L. Wei for providing the data of the reference DNS.

We acknowledge that the results of this research have been achieved using the computational resources made available at CINECA (Italy) by the high performance computing projects ISCRA-C HP10C2YR5F .

References

[1] Smagorinsky J. General circulation experiments with the primitive equations: part I, the basic experiment. Monthly Weather Review. 1963;91:99–162.

[2] Germano M. Turbulence: the filtering approach. Journal of Fluid Mechanics. 1992; 238:325–336.

[3] Sagaut P. Large eddy simulation for incompressible flows: An introduction. Springer Verlag; 2006.

[4] Deardorff J. A numerical study of three-dimensional turbulent channel flow at large reynolds numbers. Journal of Fluid Mechanics. 1970;41:453–.

[5] Scotti A, Meneveau C, Lilly D. Generalized Smagorinsky Model for Anisotropic Grids. Physics of Fluids. 1993;5(9):2306–2308.

[6] Farhat C, Rajasekharan A, Koobus B. A dynamic variational multiscale method for large eddy simulationson unstructured meshes. Comput Methods Appl Mech Engrg. 2006; 195:1667–1691.

[7] Knight D, Zhou G, Okong'o N, et al. Compressible large eddy simulation using unstructured grids. American Institute of Aeronautics and Astronautics; 1998. Report No.: 98-0535.

[8] John V, Kindl A. Numerical studies of finite element Variational Multiscale Methods for turbulent flow simulations. Computer Methods in Applied Mechanics and Engineering. 2010;199:841–852.

[9] Colosqui C, Oberai A. Generalized smagorinsky model in physical space. Computer and Fluids. 2008;37:207–217.

[10] Sengupta K, Mashayek F, Jacobs G. Large eddy simulation using a discontinuos galerkin spectral method. In: 45th AIAA Aerospace Sciences Meeting and Exhibit; AIAA-2007-402. AIAA; 2007.

[11] Moussaed C, Wornom S, Salvetti MV, et al. A modal-based multiscale method for large eddy simulation. Acta Mech. 2014;225:3309–3323.

[12] Bardina J, Ferziger J, Reynolds W. Improved subgrid scale models for large eddy simulation. AIAA paper. 1980;80:1357.

[13] Bardina J, Ferziger J, Reynolds W. Improved turbulence models based on large eddy

simulation of homogeneous, incompressible, turbulent flows. NASA NCC 2-15 report. 1983;TF-19.
[14] der Bos F, van der Vegt J, Geurts B. A multi-scale formulation for compressible turbulent flows suitable for general variational discretization techniques. Computer Methods in Applied Mechanics and Engineering. 2007;196:2863–2875.
[15] Abbà A, Cercignani C, Valdettaro L. Analysis of Subgrid Scale Models. Computer and Mathematics with Applications. 2003;46:521–535.
[16] Abbà A, Bonaventura L, Nini M, et al. Dynamic models for Large Eddy Simulation of compressible flows with a high order DG method. Computers & Fluids. 2015;122:209–222.
[17] Germano M, Piomelli U, Moin P, et al. A Dynamic Subgrid-Scale Eddy Viscosity Model. Physics of Fluids. 1991;3(7):1760–1765.
[18] Wei L, Pollard A. Direct numerical simulation of compressible turbulent channel flows using the Discontinuous Galerkin method. Computers and Fluids. 2011;47:85–100.
[19] FEMilaro, a finite element toolbox [Internet]. ???? Available from: `https://bitbucket.org/mrestelli/femilaro/wiki/Home`.
[20] Banerjee S, Krahl R, Durst F, et al. Presentation of anisotropy properties of turbulence, invariants versus eigenvalue approaches. J Turb. 2007;8:1.
[21] Almeida G, Durao D, Heitor M. Wake flows behind two-dimensional model hills. Experimental Thermal an Fluid Science. 1999;3:87–101.
[22] Breuer M, Peller N, Rapp C, et al. Flow over periodic hill - numerical and experimental study in a wide range of reynolds numbers. Computer & Fluids. 2009;38:33–457.
[23] Frölich J, Mellen C, Rodi W, et al. Highly resolved large-eddy simulation of separated flow in a channel with streamwise periodi constrictions. Journal of Fluid Mechanics. 2005; 526:19–66.
[24] Mellen C, Frölich J, Rodi W. Large eddy simulation of the flow over periodic hills. In: 16th IMACS World Congress; 2000.